

RESEARCH ARTICLE

10.1002/2015JA021828

Key Points:

- Primary modes of ionospheric conductance variability characterized as empirical orthogonal functions
- EOFs 1–4 capture a fundamental observational-based picture of ionospheric conductance variability
- First large-scale analysis of conductances free of assumption of incident electron energy spectra

Correspondence to:

R. McGranaghan,
ryan.mcgranaghan@colorado.edu

Citation:

McGranaghan, R., D. J. Knipp, T. Matsuo, H. Godinez, R. J. Redmon, S. C. Solomon, and S. K. Morley (2015), Modes of high-latitude auroral conductance variability derived from DMSP energetic electron precipitation observations: Empirical orthogonal function analysis, *J. Geophys. Res. Space Physics*, *120*, 11,013–11,031, doi:10.1002/2015JA021828.

Received 19 AUG 2015

Accepted 1 DEC 2015

Accepted article online 15 DEC 2015

Published online 23 DEC 2015

Modes of high-latitude auroral conductance variability derived from DMSP energetic electron precipitation observations: Empirical orthogonal function analysis

Ryan McGranaghan¹, Delores J. Knipp^{1,2}, Tomoko Matsuo^{3,4}, Humberto Godinez⁵, Robert J. Redmon⁶, Stanley C. Solomon², and Steven K. Morley⁷

¹Aerospace Engineering Sciences, University of Colorado, Boulder, Colorado, USA, ²High Altitude Observatory, National Center for Atmospheric Research, Boulder, Colorado, USA, ³Cooperative Institute for Research in Environmental Sciences, Boulder, Colorado, USA, ⁴National Oceanic and Atmospheric Administration, Boulder, Colorado, USA, ⁵Applied Mathematics and Plasma Physics (T-5), Los Alamos National Laboratory, Los Alamos, New Mexico, USA, ⁶National Oceanic and Atmospheric Administration/National Geophysical Data Center, Boulder, Colorado, USA, ⁷Space Science and Applications (ISR-1), Los Alamos National Laboratory, Los Alamos, New Mexico, USA

Abstract We provide the first ever characterization of the primary modes of ionospheric Hall and Pedersen conductance variability as empirical orthogonal functions (EOFs). These are derived from six satellite years of Defense Meteorological Satellite Program (DMSP) particle data acquired during the rise of solar cycles 22 and 24. The 60 million DMSP spectra were each processed through the Global Airlglow Model. Ours is the first large-scale analysis of ionospheric conductances completely free of assumption of the incident electron energy spectra. We show that the mean patterns and first four EOFs capture ~50.1 and 52.9% of the total Pedersen and Hall conductance variabilities, respectively. The mean patterns and first EOFs are consistent with typical diffuse auroral oval structures and quiet time strengthening/weakening of the mean pattern. The second and third EOFs show major disturbance features of magnetosphere-ionosphere (MI) interactions: geomagnetically induced auroral zone expansion in EOF2 and the auroral substorm current wedge in EOF3. The fourth EOFs suggest diminished conductance associated with ionospheric substorm recovery mode. We identify the most important modes of ionospheric conductance variability. Our results will allow improved modeling of the background error covariance needed for ionospheric assimilative procedures and improved understanding of MI coupling processes.

1. Introduction

Understanding the extent and nature of variance in the space environment is extremely important to our ability to predict this complex system. Therefore, a major space physics and space weather challenge is the development of succinct relationships between geospace variability and the solar and geomagnetic drivers. Here we characterize dominant modes of auroral variability and their relationship to drivers by comprehensively data mining 60 million 1 s satellite particle spectra data. Specifically, the primary modes of ionospheric Hall and Pedersen conductance variability are characterized as empirical orthogonal functions (EOFs). Ours is the first large-scale analysis of directly calculated ionospheric Hall and Pedersen conductances completely free of assumption of the incident electron energy spectra. Further, this is a first time that a comprehensive principal component analysis has been applied to satellite particle precipitation data, yielding a number of new physical insights into the auroral processes summarized in the paper. Given the extent to which EOFs have advanced our knowledge of the atmospheric and space sciences [Hannachi *et al.*, 2007, and references therein], the EOFs presented here are an important advancement for our understanding of auroral processes and magnetosphere-ionosphere coupling.

The ionospheric electrical conductivity tensor ($\vec{\sigma}$) relates electric fields (\mathbf{E}), largely imposed from outside of the ionosphere, to the current density (\mathbf{J}). In turn, these currents carry energy and their closure in the ionosphere results in significant amounts of momentum and electrodynamic energy transfer throughout the magnetosphere-ionosphere-thermosphere (MIT) system. Coupling in the MIT system and the resulting distributions of ionospheric electrodynamics and MI system configurations are thus extremely sensitive to the ionospheric conductivity [Kamide and Richmond, 1982; Kamide *et al.*, 1986, 1989; Ridley *et al.*, 2004,

Ridley et al., 2004; Zhang et al., 2004; Kihn and Ridley, 2005; Wiltberger et al., 2009; Lotko et al., 2014]. Conductivity is often integrated over altitude, allowing a volume current to be represented as a horizontal ionospheric current at an ionospheric reference altitude, typically 110 km [Chapman and Bartels, 1940; Nagata and Fukushima, 1971; Kamide et al., 1981]. Altitude-integrated conductivity is called conductance (Σ). Conductivity and conductance are two of the most important, yet uncertain, parameters in MIT specification.

Conductance depends directly on the level of solar photoionization and auroral particle impact ionization. Robinson and Vondrak [1984] connected solar ionization to conductance via parameters such as the solar zenith angle, season, and level of solar flux ($F_{10.7}$). Relationships between auroral particle precipitation and conductance are more complex and require determination of an appropriate functional form for the high-latitude particle precipitation, which is often assumed to be Maxwellian [Robinson et al., 1987; Fuller-Rowell and Evans, 1987]. Here we report application of the GLocal airglOW (GLOW) model [Solomon et al., 1988] to 60 million (6×10^7) energy flux spectra to calculate conductivity and conductance. These calculations, based on directly measured energetic particle spectra from the Defense Meteorological Satellite Program (DMSP) satellites, allow us to bypass the Maxwellian assumption. This important improvement to conductivity modeling [Christon et al., 1991; Aksnes et al., 2002; Hardy et al., 2008; McIntosh and Anderson, 2014] permits a robust calculation of the ionospheric Pedersen and Hall conductances.

The objective of this paper is to characterize primary modes of conductance variability as described by empirical orthogonal functions (EOFs) and to interpret them geophysically. EOF analysis is a member of the family of principal component analysis (PCA) or the Natural Orthogonal Component algorithms, originally described by Pearson [1901]. The objective is to reduce the dimensionality of a data set consisting of multiple intercorrelated variables, while preserving the maximum variation [Jolliffe, 2002; Wilks, 2011; A et al., 2012]. The result of PCA is a set of base functions, or EOFs, where each succeeding function is orthogonal to all previously estimated functions and describes as much variance present in the data as possible.

EOFs of the Hall and Pedersen conductances, herein represented using the polar cap spherical harmonics basis, are obtained by a sequential nonlinear regression analysis of observations along DMSP satellite trajectories and ordered by their variance. These EOFs and their amplitudes can be used to describe the spatial and temporal coherence of the Pedersen and Hall conductances in a manner similar to that reported by Matsuo et al. [2002, 2005] and Cousins et al. [2013a, 2013b] for electric field variability and Cousins et al. [2015a, 2015b] for field-aligned current variability. Our results allow for improved modeling of the background error covariance needed for ionospheric assimilative procedures [Richmond and Kamide, 1988; Matsuo et al., 2005]. Here we present the dominant modes of variability of the ionospheric conductance derived from 60 million DMSP particle observations in 1987 and 2010.

This paper is laid out as follows: section 2 details the data and methodology we use to create the EOFs. In section 3 we provide the results, which are then discussed and expanded upon in section 4. Finally, we conclude with the primary findings and significance of the work in section 5.

2. Methodology and Data

2.1. Introduction to Methodology

Here we describe the version of empirical orthogonal function (EOF) analysis that applies to sparse and irregularly spaced data.

The EOF method in this work is different from the classical PCA technique, which carries out an eigenvalue decomposition on the variance-covariance matrix for a particular set of observations. Rather, in light of the sparsity and irregularity of the data (see section 2.2), we take the approach laid out in James et al. [2000] and Matsuo et al. [2002] in which a “reduced rank, mixed effects model” is used. This method attempts to directly estimate the EOFs rather than estimating them from the full covariance matrix and subsequent eigenvalue decomposition. In order to perform a direct estimation, the observations are represented by an additive model, consisting of the overall mean ($\bar{\Sigma}$ in this study) and a truncated set of EOFs (i.e., $\sum_v \mathcal{E}OF^{(v)}$). Each term in the model is estimated sequentially after the contribution from each previously estimated term is removed. We provide the mathematical formalism for this next.

We define the conductance variability as a residual field which encompasses all perturbations from the mean conductance:

$$\Sigma' = \Sigma - \bar{\Sigma}. \quad (1)$$

We decompose the conductance variability at a given time t into dominant modes represented by EOFs (i.e., principal components):

$$\Sigma'(\mathbf{r}, t) = \alpha^{(1)}(t) \cdot \mathcal{E}\mathcal{O}\mathcal{F}^{(1)}(\mathbf{r}) + \dots + \alpha^{(v)}(t) \cdot \mathcal{E}\mathcal{O}\mathcal{F}^{(v)}(\mathbf{r}) + \mathbf{e}'(\mathbf{r}, t), \quad (2)$$

where \mathbf{r} denotes spatial position (magnetic latitude (MLAT) and magnetic local time (MLT)), $\alpha^{(v)}(t)$ are time-dependent coefficients of the v th EOF, and $\mathbf{e}'(\mathbf{r}, t)$ is the residual after removing the mean and sum of weighted EOFs from Σ . Essentially, EOFs represent 2-D time-invariant spatial modes of conductance variability and $\alpha^{(v)}(t)$ represent temporal modes that scale the spatial modes in time.

2.2. Data Set

We perform EOF analysis on conductances obtained from the GLOW model driven with DMSP spacecraft electron precipitation measurements. The DMSP spacecraft fly in polar orbits at ~ 850 km altitude with orbital periods between 90 and 105 min [Rich *et al.*, 1985]. We use the in situ electron precipitation observations from the Special Sensor J versions 4 (SSJ/4) and 5 (SSJ/5) instruments [Hardy *et al.*, 1984; Kadinsky-Cade *et al.*, 2004]. Data processing of the count rates from both versions of the instrument provides complete electron and ion energy spectra recorded every second for energies between 30 eV and 30 keV in 19 logarithmically spaced bins. We only use spectra poleward of $|45^\circ|$ MLAT to ensure that the SSJ instruments are pointed near the local zenith, which is inside the bounce loss cone at DMSP orbital altitudes above $|45^\circ|$ MLAT, thus sampling the Earthward streaming particles. In this high-latitude region, the spatial resolution of the precipitation observations is $\sim 0.1^\circ$ in latitude. Further details of the electron precipitation data and its preparation can be found in Hardy *et al.* [2008]. In terms of the calibration of these instruments, the DMSP spacecraft each undergo an in-flight calibration (IFC) procedure [Emery *et al.*, 2006]. As a means of intersatellite calibration the average IFC factor across all SSJ/4 and SSJ/5 instruments is used as a reference with which to normalize the individual IFC factors (R. Redmon and E. Holeman, personal communication, 2015).

For this study, we process six satellite years of DMSP in situ energetic electron precipitation observations to create a data set of more than 60 million raw spectra, at 1 s cadence in the specified high-latitude region, from which to estimate mean patterns and EOFs. The six years are provided by DMSP satellites F6–F8 during 1987 and F16–F18 during 2010. The choice of temporal coverage was driven by two factors: (1) DMSP orbital planes that spanned most magnetic local time sectors and (2) sufficiently broad levels of geomagnetic activity to capture the different modes of variability. Figures 1a–1d show the spatial coverage in both hemispheres by these two sets of satellites in altitude-adjusted corrected geomagnetic (AACGM) coordinates [Baker and Wing, 1989].

We analyzed solar activity data ($F_{10.7}$ and sunspot number, Figures 1e and 1f, respectively) and geomagnetic indices (Kp and AE , Figures 1g and 1h, respectively) from NASA OMNIWeb for 1987 and 2010. Figures 1e–1h show that while the $F_{10.7}$ index is quite similar for 1987 and 2010, the sunspot number and level of geomagnetic activity are considerably higher for 1987. Dashed blue and red lines, respectively, show yearly quartiles in 1987 and 2010 in Figures 1e–1h. The data spread is greater in 1987 than 2010 for all parameters, indicating more large storms and deeper quiet periods in 1987. To reduce ionospheric preconditioning complications from generally heightened solar background, we chose data from near solar minimum (Sunspot Index and Long-term Solar Observations data/image, Royal Observatory of Belgium, Brussels, <http://www.sidc.be/silso>) which correspond to periods of low-to-moderate solar activity. A likely difference between these data and solar maximum data is the peak values in the mean conductance patterns, given the level of solar irradiance.

In order to represent the primary modes of variability in a single set of EOFs, we do not bin the observations by geomagnetic activity. This choice was governed by our primary objective, which is to create a set of EOFs that can be used in data assimilative procedures as a compact representation of the background model error covariance for ionospheric conductances. Moreover, this allows us to discuss the overall primary modes of variability rather than those associated with specific levels of activity. This approach lends itself to more general application.

We focus exclusively on the electron precipitation in this work. Proton precipitation and associated conductivity can be significant under specific conditions and in certain locations, such as the equatorward boundary of the auroral zone near midnight local time [Galand and Richmond, 2001]. Extending our analysis to include protons is left as future work.

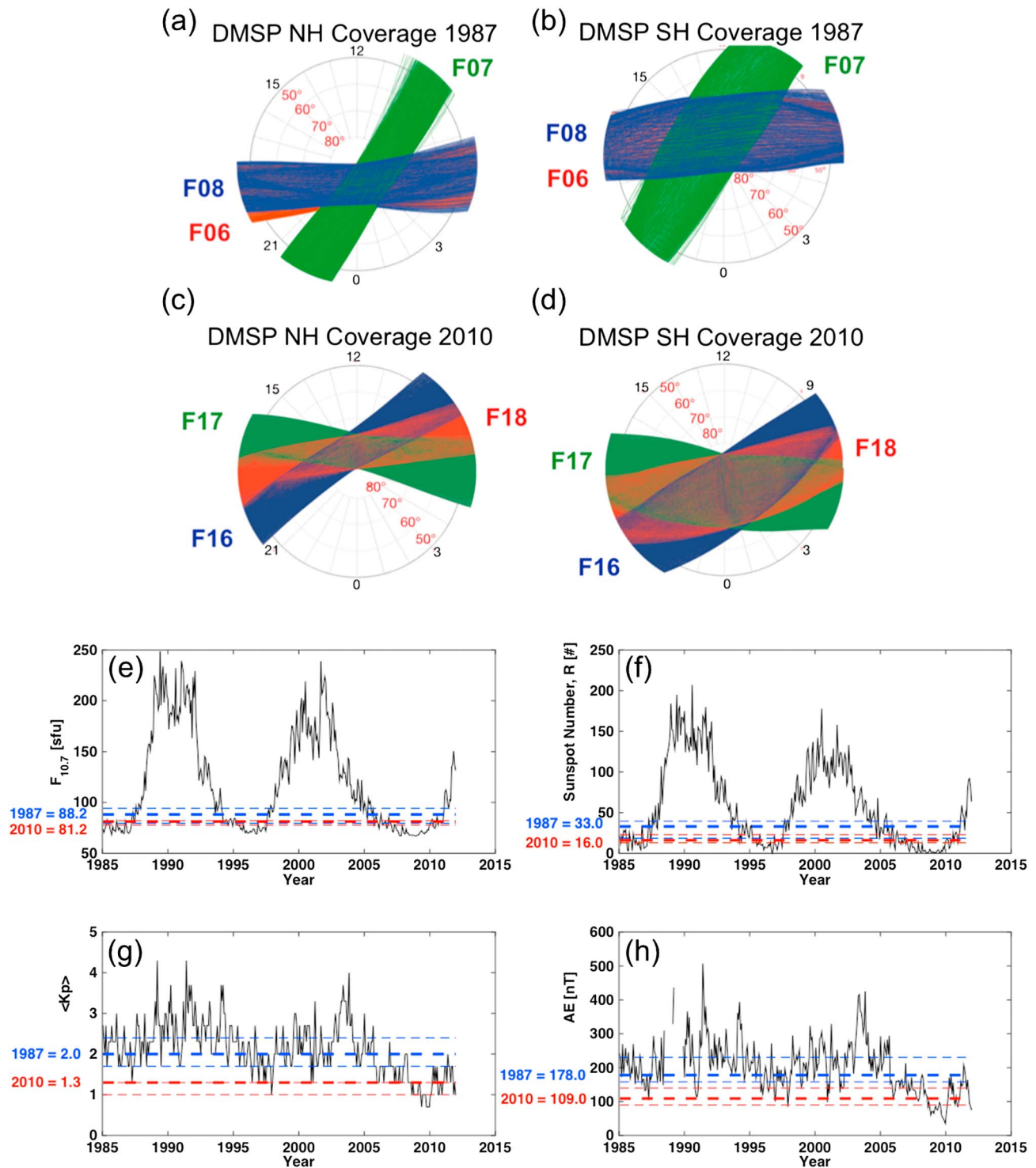


Figure 1. (a–d) Spatial coverage from the DMSF F6–F8 (1987) and F16–F18 (2010) satellites for EOF construction, in magnetic coordinates. Northern and Southern Hemisphere coverage provided in (Figures 1a and 1b) 1987 and (Figures 1c and 1d) 2010. (e–h) Temporal coverage from the DMSF satellites showing solar and geomagnetic activity comparisons in 1987 and 2010. Twenty-seven day averages from 1985 to 2012 for: (Figure 1a) $F_{10.7}$ index (solar flux unit), (Figure 1b) sunspot number, (Figure 1c) Kp index, and (Figure 1d) AE index (nT). The median, upper, and lower quartile values are shown by the dashed lines for 1987 (blue) and 2010 (red). The values to the left of Figures 1e–1h) represent the medians.

2.3. Global Airglow (GLOW) Model

The GLOW model is used to determine the effects due to precipitating auroral and photoelectron fluxes on the ionosphere [Solomon *et al.*, 1988; Solomon and Abreu, 1989; Bailey *et al.*, 2002]. GLOW adopts a radiative transfer method of calculating these effects and implements the two-stream electron transport code of Nagy and Banks [1970]. Background neutral and ionized atmospheres are calculated using the Mass Spectrometer and Incoherent Scatter Radar model [Picone *et al.*, 2002] and International Reference Ionosphere (IRI) model [Bilitza, 1990], respectively. IRI electron density profiles are supplied to ensure stability of the electron transport calculation but are subsequently replaced by the calculated electron densities below 200 km altitude. Therefore, IRI profiles are not used in the final conductance calculations. We use the GLOW model to calculate ionization and dissociation rate profiles, ion and electron densities, and height-resolved Pedersen and Hall conductivities [Solomon *et al.*, 1988]. GLOW computes ion and electron densities under the assumption of photochemical equilibrium. The photochemical equilibrium assumption is generally good below 200 km. Further discussion of this point is provided by Richards *et al.* [2010]. Calculations of the Pedersen and Hall conductivities are performed using

$$\sigma_P = \frac{q_e}{B} \left[N_{O^+} \frac{r_{O^+}}{1 + r_{O^+}^2} + N_{O_2^+} \frac{r_{O_2^+}}{1 + r_{O_2^+}^2} + N_{NO^+} \frac{r_{NO^+}}{1 + r_{NO^+}^2} + N_e \frac{r_e}{1 + r_e^2} \right] \quad (3)$$

$$\sigma_H = \frac{q_e}{B} \left[-N_{O^+} \frac{1}{1 + r_{O^+}^2} - N_{O_2^+} \frac{1}{1 + r_{O_2^+}^2} - N_{NO^+} \frac{1}{1 + r_{NO^+}^2} + N_e \frac{1}{1 + r_e^2} \right], \quad (4)$$

where

$$r_x = \frac{\text{collision frequency}}{\text{gyrofrequency}} = \frac{v_x}{\omega_x} \quad (5)$$

$$\omega_x = \frac{q_e B}{m_x}. \quad (6)$$

Here q_e is the magnitude of the charge of an electron, B is magnetic field strength, m_x is mass, and N_x is number density. Collision frequencies are obtained from Schunk and Nagy [2009]. For this study we integrate the conductivity profiles over 80–200 km altitude to yield ionospheric conductances. Because they are not directly observed but are fed to the estimation procedure as observations, they are hereafter referred to as pseudo-observations. Only conductance EOFs integrated between 80 and 200 km are presented here, but our methods are easily applied to conductance and conductivity determination at specific altitudes and altitude ranges.

GLOW contains a background source of ionization separate from the solar and auroral precipitation sources: the background “nighttime” ionization. The background ionization was designed to conform to the Thermosphere-Ionosphere General Circulation Model [Roble *et al.*, 1988] and takes into account fluxes from the stellar background and multiple scattering of solar atomic hydrogen emissions in the geocorona [Strobel *et al.*, 1980]. The background ionization is small compared with that created by precipitating particles and the effect on these results is not significant except to ensure a nonzero level of ionization, and thus nonzero conductances, at all times.

Further details about the GLOW code can be found in Solomon *et al.* [1988] and McGranaghan *et al.* [2015].

2.4. Empirical Orthogonal Functions (EOFs) and Related Data Processing

We fit the pseudo-observations to the same spherical cap harmonics basis functions used in the assimilative mapping of ionospheric electrodynamics procedure [Richmond and Kamide, 1988]. These basis functions are generalized Legendre functions at high latitudes with appropriate low-latitude extensions that satisfy a zero Laplacian requirement. We select the 50 basis functions that represent the first 50 principal modes in the background error covariance also developed in that work. The resolution of the basis functions is roughly 2.5°.

The nonlinear regression analysis to determine each EOF is performed by minimizing the following cost function [Matsuo *et al.*, 2002]:

$$L^{(v)} = \sum_t^T \sum_r^R \left[\mathbf{y}_{rt}^{(v)} - \alpha_t^{(v)} \sum_k^K \beta_k^{(v)} \mathbf{x}_{krt} \right]^2 + \lambda \sum_k^K |\beta_k|, \quad (7)$$

where

v = EOF number;

$\mathbf{Y}_{rt}^{(v)}$ = vector containing R residual pseudo-observations at a location r in an EOF analysis block t ;

$\alpha_t^{(v)}$ = weighting factor for EOF analysis block t ;

$\beta_k^{(v)}$ = regression coefficient;

\mathbf{X}_{krt} = k th basis function evaluated at location r in an EOF analysis block t ;

K = number of basis functions chosen;

$\lambda \sum_k^K |\beta_k|$ = L^1 norm penalty term and λ is the nonnegative regularization parameter.

The process is nonlinear because the spatial coefficients, $\beta_k^{(v)}$, and temporal coefficients, $\alpha_t^{(v)}$, are estimated iteratively. An EOF “analysis block” is defined as a 1 h period over which all available DMSP observations are accumulated and represents the resolution of the temporal modes (e.g., α).

The highly variable nature of ionospheric conductivities introduces significant stability issues in the EOF estimation process. We used the Least Absolute Shrinkage and Selection Operator (LASSO) [Tibshirani, 1996] regularization to handle this instability. Generally, LASSO introduces an L^1 norm penalty term ($\lambda \sum_k^K |\beta_k|$ in equation (7)) to the least squares estimation and therefore minimizes the sum of the squared errors plus the absolute value of the regression coefficients. The tuning parameter, λ , determines the amount of regularization, where the limiting case of $\lambda = 0$ yields the nonregularized optimization solution. LASSO regularization is most applicable in situations where there are a moderate number of mesoscale effects, and thus LASSO is deemed appropriate for the objectives of this study.

The typical scaling convention used in principal component analysis, $\sum_k^K (\beta_k^{(v)})^2 = 1$, is applied to circumvent the nonuniqueness of the analysis (the equations are still valid if a constant is multiplied throughout) along with a constraint to force orthogonality:

$$\sum_k^K \beta_k^{(v)} \beta_k^{(v-n)} = 0 \quad n = 1, \dots, v - 1. \quad (8)$$

A suitable mean, which is invariant with time, must be calculated and removed from the data before the EOF calculations can be performed. We calculate the mean, or $\sum_k^K (\beta_k^{(0)} \mathbf{X}_{krt})$, through a linear minimization regression of $L^{(0)}$ in equation (7) with $\alpha_t^{(0)} = 1$ and the constraint on $\beta_k^{(0)}$ shown in equation (8) lifted.

The EOFs are then computed from these residual data in a sequential manner. For instance, the first EOF depends on pseudo-observations with the mean component removed, $\mathbf{Y}_{rt}^{(1)} = \mathbf{Y}_{rt}^{(0)} - \sum_k^K (\beta_k^{(0)} \mathbf{X}_{krt})$ and is estimated using regression on equation (7). The cost function is smooth in this work and thus defining a set number of iterations is sufficient to obtain convergence. Once an EOF is found, three steps are taken: (1) its contribution to the pseudo-observations is removed; (2) a Gram-Schmidt orthogonalization [Demmel, 1997] transforms the new residual set to a space orthogonal to all previous EOFs (equation (8)); and (3) equation (7) is minimized to identify the next EOF. Orthogonality is enforced during the iterative fitting procedure. We determine the maximum order (v) of the EOF series as those components that describe 50% of the variability in the data, which yields $v = 4$ in this work. This is also the point at which the percentage variation described by subsequent individual EOFs falls below 5% and is thus deemed an appropriate number of EOFs to analyze in this manuscript.

To demonstrate the effect of regularization, we provide a comparison of mean Hall conductance patterns without (Figure 2a) and with (Figure 2b) regularization. In Figure 2 (and subsequent figures below) the region interior to the solid black curves on each polar plot delineate areas well supported by observations. Structure outside of these lines are artifacts of the estimation procedure. Clearly the nonregularized pattern can yield nonphysical negative conductances (note the different color axes limits) where the estimation is not constrained. These can then inappropriately influence estimation even within the observational bounds. The LASSO regularization successfully stabilizes the estimation while still capturing the important geophysical

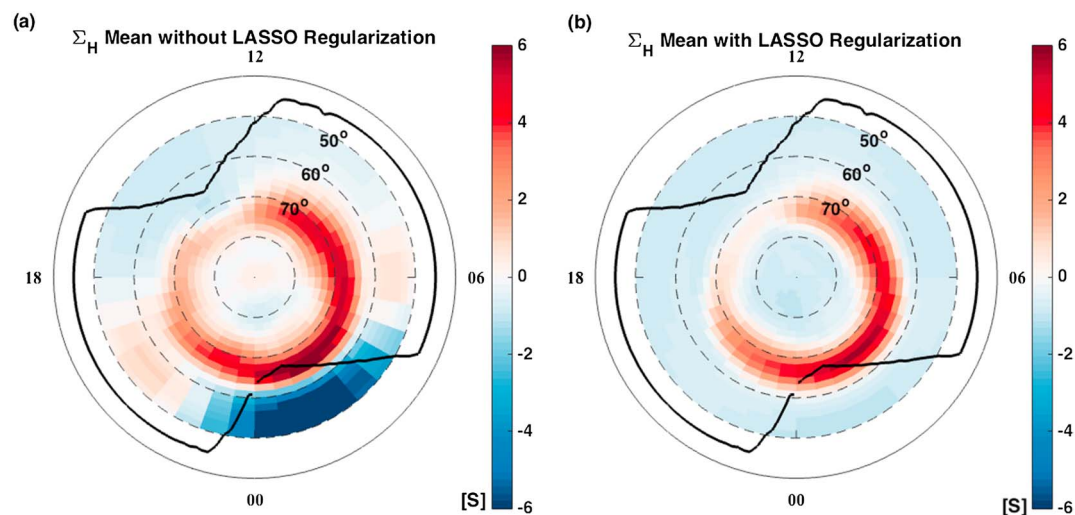


Figure 2. Mean Hall conductance patterns. (a) Without regularization and (b) with LASSO regularization.

features present in the nonregularized result (primarily the auroral oval structure). The LASSO slightly mutes some features, which results from regularization in general.

The DMSP conductance pseudo-observations require additional processing prior to being used in this estimation. They were averaged over 60 s (roughly 4° MLAT) to produce ~22 averaged pseudo-observations from each of the ~28 daily polar passes. After accounting for missing data in the DMSP databases, we processed roughly 40,000 high-latitude passes, resulting in over a million pseudo-observations (~60 million 1 s spectra each providing one pseudo-observation, which are averaged over 60 s) with fairly even seasonal distribution. Data processed in this manner yield variability on mesoscale and global scale.

We provide Figure 3 to detail the observational characteristics. Figure 3a shows the distribution of data counts in the Northern and Southern Hemispheres during the 24 month period of interest, including the 60 s averaged pseudo-observations resolved on an equal-area grid for easy visual interpretation. In estimating the EOFs we use the pseudo-observations at their actual geomagnetic coordinates. We assumed hemispheric conjugacy in order to provide sufficient data coverage in MLAT and MLT. Despite the conjugacy assumption, Figure 3 shows that the magnetic local time coverage of the F6–F8 and F16–F18 satellites is not complete, lacking pseudo-observations in the low latitudes in premidnight to postmidnight and postnoon local time sectors. These data gaps can create estimation instability in the EOF regression procedure and are further motivation for the use of regularization. Figures 3b and 3c show bin-averaged Hall and Pedersen conductances, respectively, in units of Siemens.

In this analysis we use the term “analysis block,” defined by t in equation (7), to refer to the 1 h time step for the EOF process. Note these analysis blocks, hereafter simply blocks, are different than a DMSP orbit over the high-latitude region. EOF blocks have a set start and end time and contain all pseudo-observations available during that period (see Figure 4e and explanation below). This choice provides a short enough window to capture the mesoscale and global-scale time variations in the data and a long enough window for sufficient data coverage to constrain the fits. One α from equation (7) is estimated for each block, while the EOFs are time invariant. Each 1 h block contained roughly 79 sixty second averaged pseudo-observations, and we processed ~14,000 hourly blocks over the course of 1987 and 2010.

Since our primary interest is the conductance variability due to precipitating particles, which is the more unsteady and uncertain component of ionospheric conductance [Reiff, 1984; Knipp, 1989; Brekke and Moen, 1993; Germany *et al.*, 1994], we excluded the solar ionization component from the GLOW calculations. Although solar ionization is excluded, the general level of solar activity impacts the GLOW model through the $F_{10.7}$ and A_p dependence of the background neutral and ionized atmospheres. In section 4 we discuss a different approach to treat solar and auroral conductance components simultaneously.

Figure 4 provides a step-by-step overview of the data and methods used in this work. In Figure 4a we show a single Northern Hemisphere pass of the DMSP F16 satellite in AACGM coordinates on 15 January 2010,

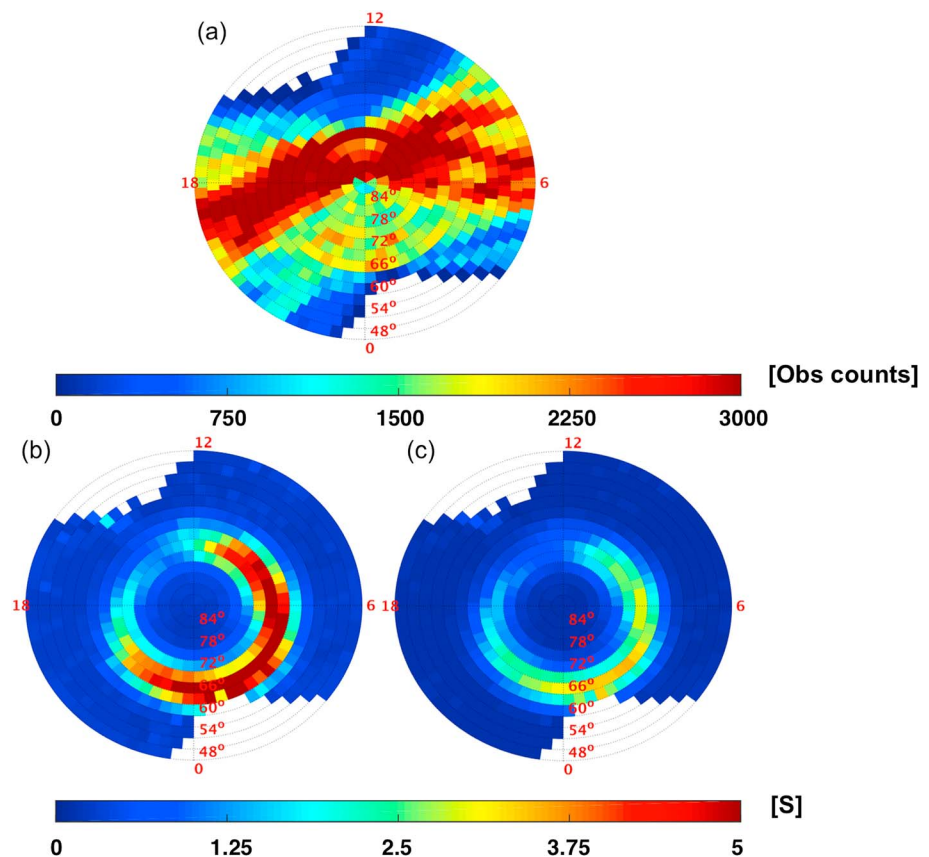


Figure 3. (a) Conductance observation density, (b) Hall conductance means, and (c) Pedersen conductance means in equal-area grids for the complete set of 60 s averaged, Northern and Southern Hemisphere pseudo-observations. Conductances means are shown in units of Siemens (S). The pseudo-observations in these bin averages are the complete data set after averaging the raw spectra, precipitated through the GLOW model.

a day used in the creation of the EOFs. Superimposed on the dusk-to-dawn satellite track are the total electron energy fluxes calculated at a 1 s cadence from the SSJ/5 instrument observations. On this very quiet day (average $Kp = 1$) there are only small enhancements in the auroral zones, which are confined to high MLATs. Figure 4b shows a sample electron energy flux spectrum observed at 80° MLAT and 14 MLT during the pass in Figure 4a. Spectra like this are calculated from SSJ observations at a 1 s cadence and are used as input to the GLOW model, resulting in conductivity profiles for that time and location. Figure 4c shows the GLOW Hall and Pedersen conductivities for this spectrum. The Hall conductivity peaks near 110 km, while the Pedersen profile has a smaller peak closer to 120 km. Each profile shows significant vertical structure.

Figure 4d gives the Hall (in blue) and Pedersen (in red) conductances along the satellite track shown in Figure 4a. The markers represent the conductances calculated at the same 1 s cadence of the SSJ/5 instrument (each marker is an altitude-integrated conductance calculated from an energetic electron spectrum (Figure 4b) and its corresponding conductivity profile (Figure 4c), and these conductances are the pseudo-observations introduced above. The dashed lines represent the 60 s smoothed averages used to drive the EOF estimation process. The conductances, even during a quiet period, are highly dynamic and introduce significant stability issues in the EOF estimation without smoothing.

Finally, Figure 4e shows how this information is used to estimate EOFs. We accumulate pseudo-observations over a 1 h estimation time step (an EOF block), corresponding to the time resolution of the EOF temporal coefficients, from all available satellites and from both hemispheres. Figure 4e shows the available pseudo-observations during the first hour on 15 January 2010, which captures the first half of the F16 orbit from Figure 4a. Data from a single block are used to estimate a single α coefficient while all data are used to estimate β coefficients.

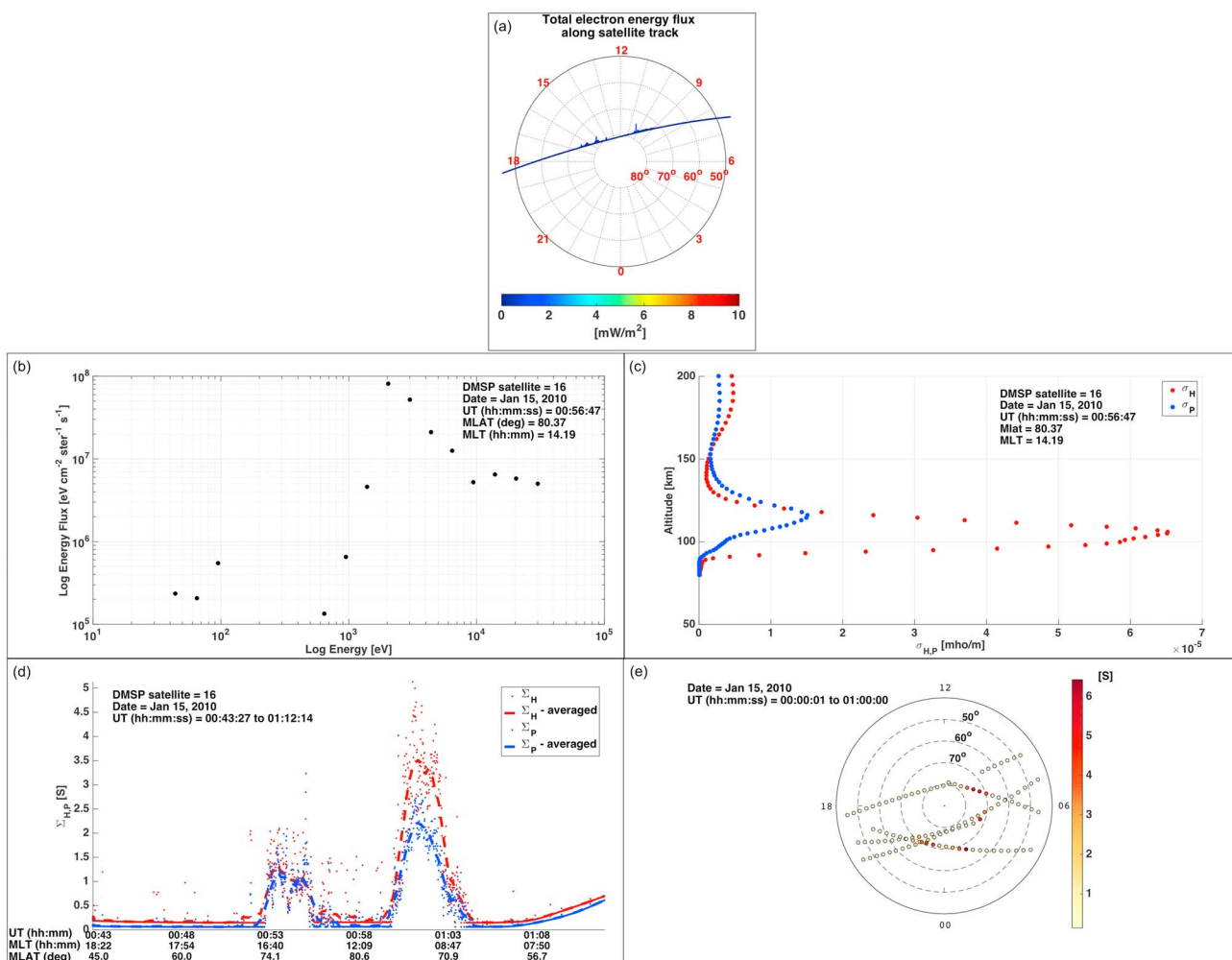


Figure 4. Overview of the observations and processing prior to EOF estimation. (a) DMSP F16 satellite Northern Hemisphere orbit on 15 January 2010 shown looking down on the North Pole with the Sun off to the top of the figure. Superimposed on the altitude-adjusted corrected geomagnetic MLAT and MLT coordinates are the total electron energy fluxes (mW m^{-2}) which are calculated at a 1 s cadence from DMSP observations. (b) Sample electron energy flux spectrum ($\text{eV cm}^{-2} \text{ster}^{-1} \text{s}^{-1} \Delta\text{eV}^{-1}$) observed during the F16 pass shown in Figure 4a). These spectra are also obtained at a 1 s cadence. (c) Hall (red) and Pedersen (blue) conductivities (S/m) calculated from the spectrum shown in Figure 4b using the GLOW model as detailed in the text. (d) Hall (red) and Pedersen (blue) conductivities (S) (integrated between 80 and 200 km) along the F16 pass shown in Figure 4a. The dots represent the values calculated at the 1 s cadence of DMSP measurements and the dashed lines represent the 60 s averages used for EOF estimation. (e) The accumulation of observations that contains the F16 pass shown in Figure 4a for EOF temporal mode estimation using a 1 h analysis time step (one EOF block is shown). Observations are accumulated from all the DMSP satellites available on this date and in this 1 h time window and include observations from both hemispheres.

3. Results

Figure 5 shows the mean and first four EOFs for the Hall (a–e) and Pedersen (f–j) conductances. We limit our discussion to areas with observational support. The maximum and minimum values for the mean of each conductance are in units of Siemens (S). Each EOF pattern is shown on a scale of -0.5 to 0.5 . The EOF signs are arbitrary since their contribution can be either added to or subtracted from the mean pattern. Hereafter, we will denote Hall and Pedersen EOFs as HEOF and PEOF, respectively.

The mean Hall and Pedersen conductance patterns (Figures 5a and 5f) capture $\sim 60\%$ of the variability and the general quiet time auroral features shown in the conductance maps in Plates 3a and 4a of Fuller-Rowell and Evans [1987], Figure 2 of Newell et al. [1996a], and Plates 10 and 12 of Ridley et al. [2004]. The patterns are generally consistent with precipitation of eastward convecting plasmasheet electrons in the postmidnight MLTs, which in turn, produce a broad crescent-shaped region of diffuse auroral electron precipitation as shown in Hardy et al. [1987] and Figure 5 of Newell et al. [2009]. This diffuse electron precipitation is the dominant contributor to the global precipitation budget [Winningham et al., 1975; Newell et al., 2009].

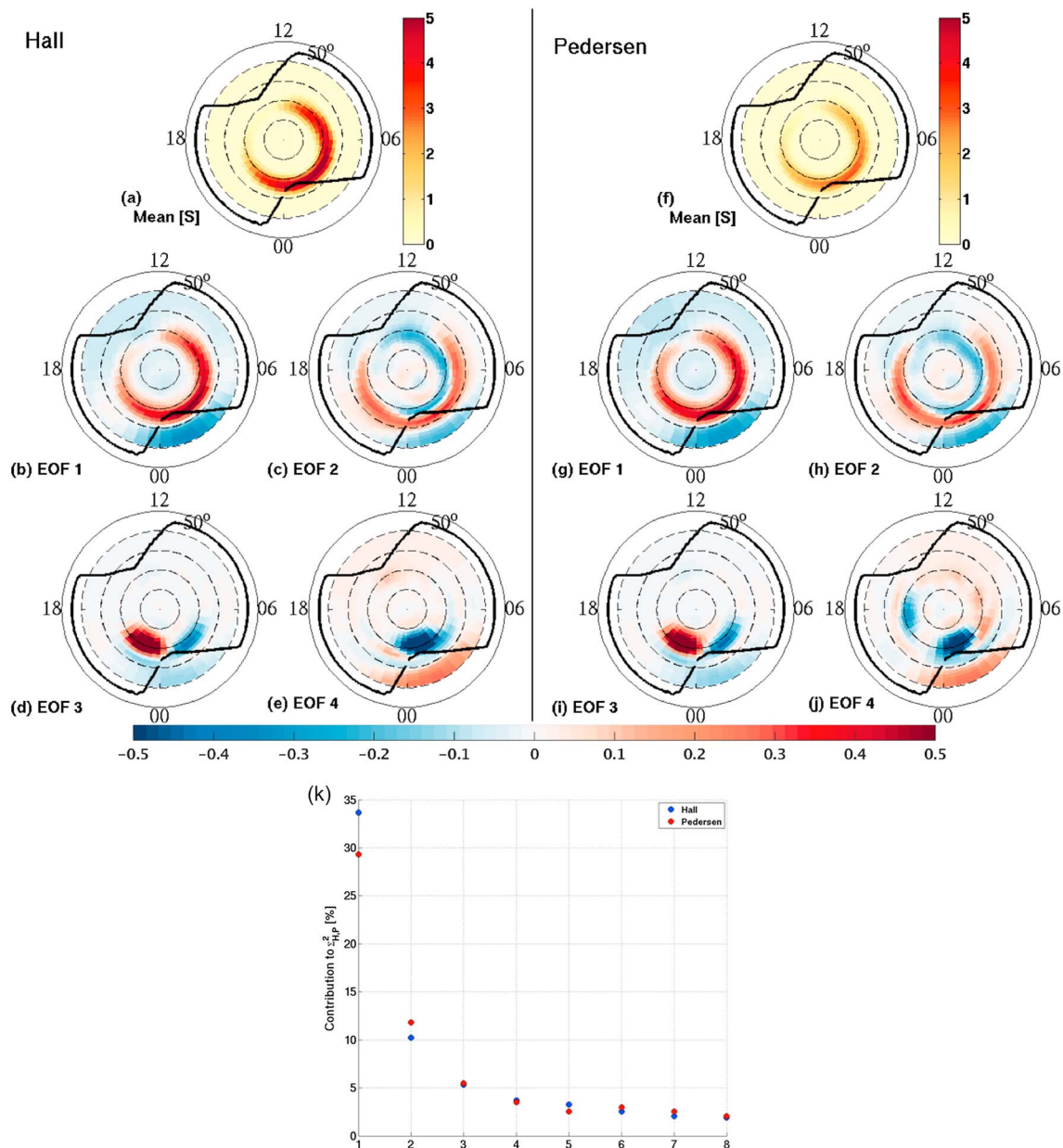


Figure 5. EOF results for the Hall and Pedersen conductances. Mean and first four EOFs for (a–e) Hall and (f–j) Pedersen conductances, in magnetic coordinates. The low-latitude limit on all polar plots is 50° and dashed lines are plotted at 10° increments up to 80°. The solid black curves indicate the boundaries of observational support. (k) Percent of the total variation in the total pseudo-observations captured by the first eight EOFs for the Hall (blue) and Pedersen (red) conductances. The first four EOFs capture 52.9% and 50.1% of the total variation for the Hall and Pedersen conductances, respectively. EOFs 5–8 describe an additional 10% for each conductance.

The patterns in HEOF1 and PEOF1, constituting ~33.7 and 29.3% of the variation, respectively, have a similar pattern to the large-scale mean conductance and likely represent a strengthening and weakening of the large-scale, quasi-permanent conductances from variability of electron precipitation in magnetic local time [Newell et al., 2009; McIntosh and Anderson, 2014].

HEOF2 (~10.2% of the overall variability) and PEOF2 (~11.8%) show an enhancement region equatorward of the location of EOF1 patterns which is most likely representative of an expansion of the auroral zone brought on by electron precipitation tied to geomagnetic activity. The enhanced component centered at midnight local time, expands beyond dusk in the westward direction and beyond dawn eastward, and remains relatively constant in latitudinal width and location, occupying latitudes between 60 and 70°. These features are characteristic of general equatorward expansion of the auroral oval with geomagnetic activity

[Hardy, 1985; Hardy et al., 1987; Fuller-Rowell and Evans, 1987; Lummerzheim et al., 1991]. There are subtle differences in the dawnside and duskside patterns. The dawnside enhanced region extends slightly further toward noon local time, but remains centered at roughly 65° MLAT. On the other hand, the duskside features subside just past 1800 MLT and show a slight trend toward higher MLATs with decreasing MLT, reaching ~70° MLAT at dusk. Finally, there is a region of opposite sign at polar latitudes extending throughout the entire dawnside.

HEOF3 and PEOF3 signify ~5% of the variability and both exhibit two strong features with opposite sense surrounding the midnight meridian. The pre-midnight component is broader in latitude, extending from ~65° to greater than 75° MLAT and covering roughly 3 h in local time. The post-midnight signature is more confined in latitude and is opposite in sign. These signatures are consistent with modulation of electron precipitation associated with the divergence of the cross-magnetotail current into the ionosphere during auroral substorms, or the substorm current wedge (SCW) [McPherron et al., 1973; Pytte et al., 1976; Elphinstone et al., 1996; Gjerloev and Hoffman, 2002; Kepko et al., 2014].

EOF4s exhibit a dominant signature in the midnight-to-postmidnight local time sector, span roughly 3 h MLT at 70° MLAT, and capture ~4% of the variability. The features in Figures 5e and 5j are smaller in scale, and likely represent a substorm recovery mode.

To ensure the efficacy of our EOF patterns, we carried out a bootstrap estimation procedure in which 40 different sets of EOFs were estimated from 40 different randomly selected subsets, comprising 2500 blocks, or roughly 200,000 pseudo-observations. Although not shown here, we find that the first two EOFs were largely invariant between each run, while the next two EOFs exhibited similar features, though not always in the same order, and some subsets contained different features in the higher orders. These results indicate that our estimation procedure is robust to the number of pseudo-observations used.

Figure 5k shows the percentage of the overall variation in the conductance pseudo-observations, Σ^2 , that is captured by EOFs 1–8 for Hall (blue markers) and Pedersen (red markers) conductances. We show the percentage variation captured by EOFs 5–8, for which the spatial patterns are not provided, to illustrate that these higher-order EOFs capture an increasingly small percentage of the overall variation in the data. The amount of variability is represented by the percent reduction in the cost function (equation (7)) when the contribution from each EOF is subtracted from the residual observations (i.e., the sum of the squared distance from the mean). The first four EOFs capture 52.9% and 50.1% for the Hall and Pedersen conductance variability, respectively. EOFs 5–8 describe an additional 10% for each conductance.

To explore the possible drivers of the dominant modes of variability represented by the EOFs in Figures 5b–5e and 5g–5j, we correlated the temporal modes, or the time series of coefficients of each EOF (α_i) which represent the strength of each EOF at a given time period, with the corresponding time series of various solar wind parameters and solar and geomagnetic indices. We computed correlations for solar wind parameters (speed, pressure, density, and magnetic field components in geocentric solar magnetic (GSM) coordinates), geomagnetic indices (auroral electrojet indices (*AE*, *AU*, and *AL*), SuperMAG indices (auroral electrojets: *SME*, *SMU*, and *SML* and ring current: *SMR*) [Newell and Gjerloev, 2011a, 2012], planetary index (*Kp*), polar cap index (*PC*), and disturbance storm time index (*Dst*)), and specialized coupling functions (the interplanetary electric field ($E_Y = -V_{SW} \times B_{Z,GSM}$), the Borovsky coupling function (CF) [Borovsky, 2013], and the Newell CF [Newell et al., 2007]).

Some aspects of the correlations are noteworthy:

1. Since indices represent imperfect proxies for ionospheric phenomena, which themselves often respond in a nonlinear manner to many different drivers, we are encouraged by the fact that several of the correlation coefficients between the indices and higher-order EOFs are greater than 0.5.
2. The more localized the EOF features, the less likely they are to be correlated with the parameters. This is why correlations generally decrease for higher-order EOFs [Matsuo et al., 2002; Cousins et al., 2013a]. Thus, low correlations do not necessarily mean a relationship does not exist. Alternatively, high correlations demonstrate a relationship exists but do not necessarily provide information about causation.
3. EOFs are not necessarily organized according to physical cause. They capture the direction of most variability in the data subject to the constraint that it is orthogonal to each previous, more prominent, direction of variability, and irrespective of the correlation with physical drivers [Cosgrove et al., 2014].

Table 1. Properties of Hall and Pedersen EOFs^a

EOF Mode	1 Strengthening/Weakening	2 Auroral Zone Broadening	3 Substorm Current Wedge	4 Recovery/Small-Scale Features
<i>Properties of the First Four Hall EOFs</i>				
Contribution to Σ_H^2	33.67	10.20	5.33	3.72
Top correlation	AE/PC: 0.60	AE: 0.72	SME/SMU: 0.17	SME: 0.21
Second correlation	AL: -0.57	AL: -0.69	AL/SML: -0.15	SML: -0.20
Third correlation	SME/Kp: 0.57	AU: 0.66	AE: 0.14	SMR: -0.19
<i>Properties of the First Four Pedersen EOFs</i>				
Contribution to Σ_P^2	29.30	11.80	5.51	3.49
Top correlation	PC: 0.56	AE: 0.78	SMU: 0.16	Kp: 0.22
Second correlation	Kp: 0.54	AL: -0.74	SME: 0.14	AU/Dst: 0.21/-0.21
Third correlation	AE: 0.54	AU: 0.73	SML/Newell: -0.11/0.11	PSW: 0.20

^aCorrelation coefficients are given for the three parameters that correlate most strongly with the EOFs. Correlations are based on a Pearson linear product-moment calculation.

Table 1 displays the top three correlations and the percentage variation described for each EOF shown in Figure 5 as well as our geophysical interpretation. The HEOF1 and PEOF1 temporal coefficients exhibit correlation magnitudes around 0.55 with the high-latitude magnetic indices. Though not tabulated, both Hall and Pedersen conductances correlate well with the Borovsky and Newell CFs (~ 0.45).

The HEOF2 and PEOF2 temporal modes are even more strongly correlated with the auroral electrojet indices than EOF1. Further, both conductances also exhibit stronger positive correlations with the Newell and Borovsky CFs (> 0.5) and strong negative correlations (~ -0.6) with the ring current indices (*Dst* and SMR), which decrease with increasing geomagnetic activity.

The EOF3 temporal modes are most strongly correlated the auroral electrojet indices, though the correlations are reduced from EOFs 1 and 2 (correlations between 0.1 and 0.2). The Newell CF, PC, and *Dst*/SMR indices exhibit similar magnitude correlations.

The spatial distribution and correlations associated with the third EOFs suggest a connection to substorm activity, which we examined further by recomputing correlations for each EOF3 after thresholding the values of the SuperMAG equivalent of the AL index, the SML index, to be less than -150 nT. In so doing, the correlations between EOF3 and the SuperMAG auroral electrojet indices increased by a small amount ($\sim 7\%$).

We also examined the magnitude of α_t coefficients for HEOF3 and PEOF3 during periods of substorms. Larger $|\alpha_t|$ s indicate the pattern is stronger at a given time. To identify substorm times, we used the SuperMAG substorm event database which gives the time of substorm expansion phase onsets as observed by the SML index [Newell and Gjerloev, 2011a, 2011b]. During substorm periods the median alpha coefficients for the HEOF3 was notably enhanced over the median calculated over all coefficients (for HEOF3: 4.5 in 1987 and 5.5 in 2010 versus 2.0 for all α s). In contrast, the PEOF3 median values showed little response (2.1 in 1987 and 2.8 in 2010 versus 2.4 for all alphas), consistent with smaller Pedersen conductance response to substorms [Gjerloev and Hoffman, 2002].

The temporal modes of HEOF4 and PEOF4 correlate with the SuperMAG auroral electrojet, *Kp*, and *Dst* indices. The patterns as shown are negative in the dominant feature near midnight LT (blue features), meaning that conductance diminishes as geomagnetic activity subsides.

4. Discussion

In this section we explore the geophysical interpretation of each EOF in more depth and outline the important paths for future work.

EOF 1: HEOF1 and PEOF1 are likely predominantly representative of central plasma sheet (CPS) precipitation which is a relatively stable feature in terms of ionospheric precipitation, varying primarily in terms of latitude and intensity with geomagnetic activity [Winningham et al., 1975; Newell et al., 2009; Thorne et al., 2010].

Electrons from the CPS have been directly associated with diffuse precipitation into the ionosphere [Sandford, 1968]. Hardy *et al.* [1987] connected the diffuse precipitation to increases in ionospheric conductivity, and Thorne *et al.* [2010] showed that resonant scattering of electrons by chorus band waves are a dominant source of diffuse precipitation. The locations of resonantly scattered electrons shown by Thorne *et al.* [2010] (their Figure 2) and the conductance maps created by Hardy *et al.* [1987] (their Plate 1 for Hall and Plate 2 for Pedersen conductances) are both consistent with our EOF1 patterns. An especially striking relationship exists between our results and Figure 2a of Thorne *et al.* [2010], which shows the diffuse auroral emissions captured by Polar Ionospheric X ray Imaging Experiment (PIXIE) measurements and demonstrates the enhancement as a function of the K_p index. We found a similar relationship between EOF1 and K_p as shown by the positive correlation in Table 1.

EOF 2: In contrast to the CPS source of diffuse electron precipitation, the boundary plasma sheet (BPS) is marked by accelerated electron precipitation and is much more variable, displaying more dependence on geomagnetic activity and leading to more structured, and in certain situations, localized ionospheric signatures [Winningham *et al.*, 1975; Newell *et al.*, 1996b]. EOFs 2 are suggestive of conductances driven by structured precipitation originating in the BPS.

HEOF2 and PEOF2 likely capture the conductance signatures of electron precipitation associated with magnetospheric convection. The temporal modes for these spatial patterns correlate well with the auroral electrojet indices (~ 0.7 – 0.8), K_p and PC (0.6), the Newell and Borovsky CFs (~ 0.5 – 0.6), and several other geoeffective parameters (≥ 0.5). The most prominent feature (Figures 5c and 5h) is an equatorward expansion of the auroral zone represented by the positive conductance region between 60° and 70° latitude and extending from predusk to midnight and to postdawn from midnight. Kamide and Kokubun [1996] showed that this convection-driven component of the auroral electrojets is dominated by high conductivity. Therefore, as activity increases and the auroral zone broadens latitudinally due to increased electron precipitation a corresponding increase in the conductance occurs. Stronger conductances permit stronger electrojets to flow, and we accordingly found large correlations between these patterns and the auroral electrojet indices. The auroral electrojet index correlations are stronger for EOF2 than EOF1, which suggests that the EOF2 patterns are more strongly associated with geomagnetic activity and with accelerated electron precipitation, while those in EOF1 are created by diffuse precipitation, though further investigation is needed.

Our EOF2s indicate a relationship with field-aligned currents (FACs), especially given that the magnetospheric convection component of the auroral electrojets has been linked to enhancements of the DP-2 FAC system [Clauer and Kamide, 1985]. FACs are carried by the inflow and outflow of ionospheric electrons, and conductivity changes are expected to be closely related. Figure 6a shows the large-scale Region-1/2 FACs during moderate (left) and strong (right) geomagnetic activity (reproduced from Iijima and Potemra [1978]). The component out of the ionosphere (shown by the white bars) represents electrons precipitating in and causes conductance enhancements. The white bars in Figure 6 and our second EOFs are generally consistent in terms of MLAT and MLT. We additionally see general agreement between our high-latitude negative conductance feature extending throughout dawnside LTs and the downward Region 1 FAC (shown by black bars and carried by electrons moving away from the ionosphere). The absence of a similar duskside feature for the low-latitude FACs could be a result of the regularization process suppressing these lower-latitude features. A correspondence between our results and large-scale Region-1/2 FACs [Iijima and Potemra, 1978] speaks to the importance of this study given that the goal is to aid in ionospheric data assimilation, in which FACs are a crucial component.

EOF 3: HEOF3 and PEOF3 suggest electron precipitation associated with the SCW [McPherron *et al.*, 1973; Pytte *et al.*, 1976; Elphinstone *et al.*, 1996; Gjerloev and Hoffman, 2002; Kepko *et al.*, 2014]. The local time extent of the pre-midnight and post-midnight features in Figures 5d and i is in general agreement with the 6 h local time (90°) width of the SCW specified in phenomenological sense by Gjerloev *et al.* [2007]. Kepko *et al.* [2014] conducted an extensive study of the SCW, including historical information, and concluded that the large-scale organization of this feature originally identified by McPherron *et al.* [1973] remains valid. In this picture, the western edge of the wedge is collocated with a region of intense upward field-aligned current (downward electron precipitation) that is the westward edge of the westward traveling surge. Sergeev *et al.* [1996] presented several case studies of optical auroral images associated with the SCW and concluded that the western bulge region is the area of brightest auroral luminosity, and it is generally accepted that the auroral bulge is the region of bright, expanding auroras associated with substorm onset. The brighter regions in

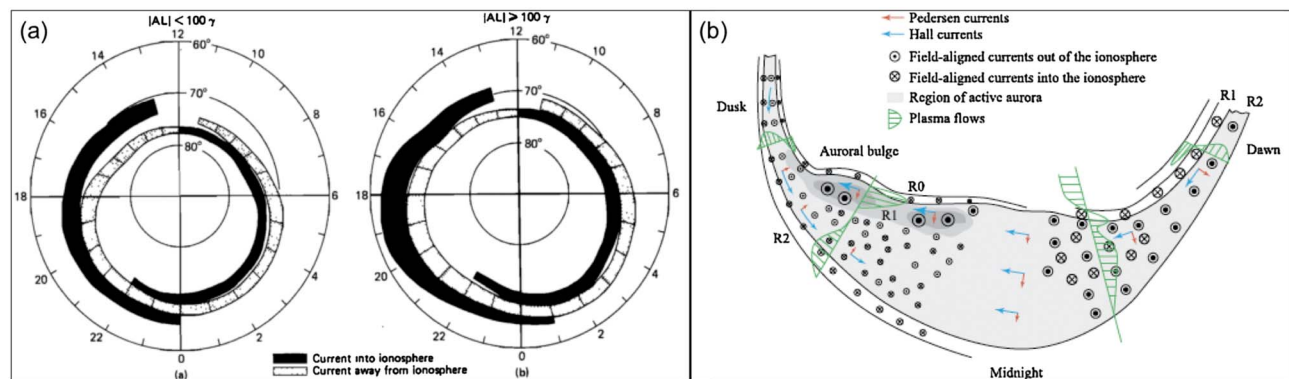


Figure 6. Reproduced figures showing the following: (a) large-scale Region-1/2 FACs during moderate (left) and high (right) geomagnetic activity (from *Iijima and Potemra* [1978]) and (b) generic isolated substorm aurora features (from *Kepko et al.* [2014]).

optical images are caused by electron precipitation which in turn cause conductance enhancements, and indeed *Kamide et al.* [1996] showed that the ionospheric electrojets in this premidnight SCW location are carried by enhanced conductances. These enhancements are realized in the premidnight signatures in both HEOF3 and PEOF3. Alternatively, *Kamide et al.* [1996] found that the postmidnight electrojets associated with the SCW were carried by a strong electric field, rather than enhanced conductances. *Davies and Lester* [1998] found a tendency in regions of moderate to strong electric field values, such as those produced in the postmidnight sector during substorms, for enhancements in the electric field to be accompanied by decreases in ionospheric conductances. We correspondingly find less pronounced and negative features in the postmidnight LT location.

The strongest auroral luminosities in the SCW signature have been shown to occur during substorm onset [*Gjerloev and Hoffman*, 2002], consistent with the premidnight signatures captured in the third EOFs. Though the latitudinal agreement is not perfect (note *Gjerloev and Hoffman* [2002] used optical images to conduct their statistical analysis of substorm onset and limited their event database through several criterion), the statistical location of onset found in that study (their Figure 6) is in remarkable agreement with the premidnight enhancement shown in our Figures 5d and 5i.

The SCW interpretation of EOF3 is supported by correlations with auroral electrojet indices and the Newell CF, through increased correlations when only periods of $AL < -150$ nT were included (a common criteria for substorm occurrence), and by enhanced temporal modes (e.g., larger α s) during periods of substorm onset as identified from SuperMAG data.

Although our EOFs, which represent averaged features, do not capture the many complexities and high variability associated with the SCW, they successfully describe the fundamental and averaged picture. Our results demonstrate that, although the MLT distribution of auroral onsets is wide, the MLT location of the SCW is quite stable and occurs primarily in the 2300 location, which is in close agreement with the findings of *Frey et al.* [2004] and *Clausen et al.* [2013]. Figure 6b shows the characteristics of a generic substorm aurora and is reproduced here from *Kepko et al.* [2014] (following from the work of *Fujii et al.* [1994] and *Gjerloev and Hoffman* [2002]). The SCW is fed by electron precipitation into the ionosphere (upward FACs) within the auroral bulge premidnight, while a region of mixed upward and downward FACs postmidnight contributes to more tenuous conductances. This agrees with our results.

Further, we know that the temporal evolution of substorms is highly variable and can be as short as a few minutes or as long as several hours [*Pellinen et al.*, 1994]. Thus, EOFs may not describe features that commonly translate and rotate in spatiotemporal space, which is common to substorm events and their ionospheric projections [*Provan et al.*, 2004]. Despite these complications, we believe these EOFs are capturing basic substorm phenomena.

EOF 4: Both HEOF4 and PEOF4 are suggestive of the substorm recovery during which the ionosphere is returning to a predisturbed state. Thus, the prominent feature at midnight to postmidnight LTs is probably associated with a different phase of the auroral substorm than the features shown in EOF3. The fact that a recovery mode is represented as primary in these results is significant given the relative lack of

attention substorm recovery has received in comparison to substorm growth and expansion [Opgenoorth *et al.*, 1994]. Consistent with recovery, conductance decreases should exhibit a correlation with geomagnetic activity indicators. The correlations of EOF4 with the SME, Kp , and Dst indices indicate this is so. Although the correlations show appropriate trends, the geophysical interpretation of such higher-order EOFs is complicated by the orthogonality constraint. Additionally, these higher-order modes capture increasingly smaller amounts of the variability in the data (specifically between 3.7% and 3.5% for HEOF4 and PEOF4, respectively). There are small-scale features apparent throughout the high-latitude regime, which become ubiquitous as the EOF order increases. This is a well-known feature of EOF analysis. Despite the diminishing size of the spatial features, these and even higher-order EOFs are likely still geophysically significant and thus important for the purposes of error covariance creation.

Notably absent from EOFs 1–4 is a dayside cusp signature. There are two reasons for this (1) highly variable geomagnetic location of the cusp [Zhou *et al.*, 2000] and (2) hemisphere-dependent response of the cusp location to the interplanetary magnetic field (IMF) B_y component. The first explanation corresponds to a weaker cusp signal in any one geomagnetic location over the course of the analysis and thus does not produce a strong response mode overall (hence it does not appear in EOFs 1–4). However, several features in higher-order EOFs are suggestive of cusp influence. The second explanation alludes to the fact that the Northern and Southern Hemisphere cusps shift oppositely in MLT in response to IMF B_y . These shifts essentially counteract in our results due to the assumption of observation conjugacy.

Although this study examines height-integrated conductances, we point out that the analysis shown in Figures 4b and 4c yields three-dimensional conductivity information and therefore permits future extension to three-dimensional study, which we will explore in a follow-on paper.

Future Work: There are five paths for future work to further constrain the estimation process: (1) determination of the sensitivity of the EOF analysis to a particular data set and regularization technique, (2) introduction of additional pseudo-observations (conductance information), (3) inclusion of ion precipitation, (4) addition of solar-induced conductance, and (5) consideration of observational errors. Items 1 and 2 can be addressed in the near term. The work of Nicolls *et al.* [2014] details additional promising regularization techniques. Additional conductance pseudo-observations may be obtained from the Fast Auroral Snapshot Explorer (FAST) particle precipitation database [Carlson *et al.*, 2001] and electron density profiles from the Constellation Observing System for Meteorology, Ionosphere, and Climate [Schreiner *et al.*, 2007; Lei *et al.*, 2007]. Conductance EOF results obtained solely from FAST pseudo-observations will be presented in a future paper.

Items 3 and 4 are midterm efforts. Proton precipitation can be significant under certain conditions and at specific locations [Galand and Richmond, 2001]. Further, we have not investigated the conductance variability due to solar EUV. The solar-induced conductance gradient across the day-night terminator causes significant estimation issues with the procedure used here. A solution is complicated by the nonlinear nature of the conductance calculations in equations (3) and (4) which precludes a simple linear addition of the solar and particle precipitation conductance components, however, using locally supported wavelets [Kozelov *et al.*, 2008] as basis functions in the estimation process offers a potential solution.

Regarding item 5, ongoing efforts at the National Geophysical Data Center [Redmon *et al.*, 2015] in cooperation with several universities will yield reliable estimates of observational uncertainties for the DMSP satellites. However, this is a long-term effort.

There are two applications in which these EOFs can be used to study specific events. In the first instance, one can reconstruct auroral conductance patterns during quiet and storm times through evaluation of equations (1) and (2) and construct a model based on EOFs as has been demonstrated for thermospheric neutral density by Lei *et al.* [2012] and for Poynting flux by Cosgrove *et al.* [2014]. In the second, these EOFs can be combined with event-specific observations and an optimal interpolation scheme to yield conductance maps for specific events, in the same way that Matsuo *et al.* [2005] and Cousins *et al.* [2013b] performed adaptive estimation of the EOF temporal modes of the ionospheric electrostatic potential. However, these applications are beyond the scope of this paper. We will specifically explore the second application in a follow-on publication.

5. Conclusions

EOFs have provided significant value to the atmospheric and space sciences [Hannachi *et al.*, 2007]. We have applied this technique to quantify the extent and nature of ionospheric conductance variance for the first time. This work represents the first application of principal component analysis to satellite particle precipitation data and, to date, the only characterization of the dominant modes of auroral variability and their relationship to drivers free of an assumption about the incident electron energy spectra. We investigate the auroral variability by directly ingesting in situ satellite measurements of high-latitude electron precipitation to the GLOW model to produce conductance pseudo-observations. We interpret the mean patterns to represent the general quiet time auroral features seen in previous statistical studies of the conductances.

Pedersen and Hall EOFs 1–4 described ~50% of the total variation in the conductance pseudo-observations. HEOF1 and PEOF1 represent intensifications of the quiet time auroral zone and can be attributed to strengthening/weakening of the diffuse precipitation-induced conductances. The hallmark of the EOF1 patterns is an extended latitudinal and longitudinal variability of the main features of the average patterns (Figures 5a and 5f). EOF2 and EOF3 likely represent two distinct components of the auroral electrojets as suggested by Baumjohann [1982] and later expanded upon by Kamide *et al.* [1996] and Kamide and Kokubun [1996]. In this interpretation EOF2 would be associated with general magnetospheric convection during southward IMF and EOF3 would be associated with the premidnight westward electrojet surge and substorm current wedge. EOF4 represents a substorm recovery mode, an important finding in light of the fact that substorm recovery has historically received less treatment than substorm growth and recovery phases [Opgenoorth *et al.*, 1994].

We have interpreted the EOFs geophysically, and find that the EOF estimation successfully captures the primary modes of variability of the Pedersen and Hall conductances reported in many previous studies within areas supported by observations, a finding that gives credence to the statistical method. We explored the possible drivers of the dominant modes of variability represented by these EOFs through correlations of the attendant temporal modes with the corresponding time series of solar wind parameters, geomagnetic indices, and specialized activity proxies. Based on the spatial patterns and temporal mode correlations, we suggest that the first four modes of conductance variations are associated with diffuse and structured precipitation, field-aligned currents, and substorm phenomena.

Thus, we have established a fundamental observational-based picture of the ionospheric conductance variability that allows us to overcome assumptions that have influenced, and in many ways limited, conductance estimation and understanding for the past three decades. To our knowledge, no such picture of the primary modes of variability has been created before. Because clear signatures of magnetosphere-ionosphere (MI) coupling processes are present in the primary modes of variability, we suggest that an error covariance model built from these EOFs will allow better representation of MI coupling in global ionospheric and magnetospheric models. This emphasizes the importance of this work and that to follow.

Future work will introduce and assimilate new sources of conductance data to produce a single set of EOF patterns for the Pedersen and Hall conductances from multiple sources with associated realistic uncertainties. Ultimately, our results will be used to create a model error covariance for ionospheric conductance that is based on observations. This work forges a path for reconstructing conductance maps during both quiet and storm time. In a subsequent paper we show in a weeklong event study that the EOF analysis is superior to other approaches for estimating full-coverage, high-latitude conductance maps. We will also apply the estimation process detailed in this study to discrete altitude levels to obtain knowledge of Pedersen and Hall conductivities thus supporting new conductivity modeling efforts needed for the next generation of assimilative ionospheric models.

References

- A, E., D. Zhang, A. J. Ridley, Z. Xiao, and Y. Hao (2012), A global model: Empirical orthogonal function analysis of total electron content 1999–2009 data, *J. Geophys. Res.*, *117*, A03328, doi:10.1029/2011JA017238.
- Aksnes, A., J. Stadsnes, J. Bjordal, N. Østgaard, R. R. Vondrak, D. L. Detrick, T. J. Rosenberg, G. A. Germany, and D. Chenette (2002), Instantaneous ionospheric global conductance maps during an isolated substorm, *Ann. Geophys.*, *20*(8), 1181–1191.
- Bailey, S. M., C. A. Barth, and S. C. Solomon (2002), A model of nitric oxide in the lower thermosphere, *J. Geophys. Res.*, *107*(A8), 1205, doi:10.1029/2001JA000258.
- Baker, K. B., and S. Wing (1989), A new magnetic coordinate system for conjugate studies at high latitudes, *J. Geophys. Res.*, *94*(A7), 9139–9143, doi:10.1029/JA094iA07p09139.

Acknowledgments

R.M.G. was partially supported by NSF Fellowship award DGE 1144083, NSF grant AGS 1025089, NASA grant NNX13AD64G, and the Vela Fellowship at the Los Alamos National Labs Space Weather Summer School. D.J.K. was partially supported by NSF grants AGS 1025089 and AGS 1144154, AFSORFA9550-12-1-0264, and NASA grant NNX13AD64G. T.M. was in part supported by NSF grants AGS 1025089 and PLR 1443703 and the NASA award NNX14AI17G. S.C.S. was supported by the National Center for Atmospheric Research, which is sponsored by the National Science Foundation. We acknowledge use of NASA/GSFC's Space Physics Data Facility's OMNIWeb service and NASA CDAWeb which provided the solar wind and DMSP 2010 data. The DMSP 1987 data can be accessed from <http://satdat.ngdc.noaa.gov/dmosp/data/>. The GLOW model code is archived on the NCAR High Performance Storage System and is available on request from Stanley C. Solomon, stans@ucar.edu. NCAR is sponsored by the NSF. The equal-area binning used in Figure 3 is performed via a routine developed by Astrid Maute at the National Center for Atmospheric Research High Altitude Observatory. We are grateful to Liam Kilcommons, Barbara Emery, and Ernie Holeman. We gratefully acknowledge the SuperMAG initiative and the SuperMAG collaborators for the index and substorm data used herein.

- Baumjohann, W. (1982), Ionospheric and field-aligned current systems in the auroral zone: A concise review, proceedings of the Topical Meeting of the (COSPAR) Interdisciplinary Scientific Commission C of the (COSPAR) Twenty-fourth Plenary Meeting, *Adv. Space Res.*, 2(10), 55–62, doi:10.1016/0273-1177(82)90363-5.
- Bilitza, D. (1990), International reference ionosphere 1990, *Tech. Rep. NSSDC/WDC-A-R and S 90-22*, Natl. Space Sci. Data Cent., Lanham, Md.
- Borovsky, J. E. (2013), Physical improvements to the solar wind reconnection control function for the earth's magnetosphere, *J. Geophys. Res. Space Physics*, 118, 2113–2121, doi:10.1002/jgra.50110.
- Brekke, A., and J. Moen (1993), Observations of high latitude ionospheric conductances, *J. Atmos. Terr. Phys.*, 55(11–12), 1493–1512, doi:10.1016/0021-9169(93)90126-J.
- Carlson, C., J. McFadden, P. Turin, D. Curtis, and A. Magoncelli (2001), The electron and ion plasma experiment for fast, in *The FAST Mission*, edited by R. F. Pfaff Jr., pp. 33–66, Springer, Netherlands., doi:10.1007/978-94-010-0332-2_2
- Chapman, S., and J. Bartels (1940), *Geomagnetism, The Int. Ser. of Monogr. on Phys.*, Clarendon Press, Oxford, U. K.
- Christon, S. P., D. J. Williams, D. G. Mitchell, C. Y. Huang, and L. A. Frank (1991), Spectral characteristics of plasma sheet ion and electron populations during disturbed geomagnetic conditions, *J. Geophys. Res.*, 96(A1), 1–22, doi:10.1029/90JA01633.
- Clauer, C. R., and Y. Kamide (1985), DP 1 and DP 2 current systems for the March 22, 1979 substorms, *J. Geophys. Res.*, 90(A2), 1343–1354, doi:10.1029/JA090iA02p01343.
- Clausen, L. B. N., J. B. H. Baker, J. M. Ruohoniemi, S. E. Milan, J. C. Coxon, S. Wing, S. Ohtani, and B. J. Anderson (2013), Temporal and spatial dynamics of the regions 1 and 2 Birkeland currents during substorms, *J. Geophys. Res. Space Physics*, 118, 3007–3016, doi:10.1002/jgra.50288.
- Cosgrove, R. B., et al. (2014), Empirical model of Poynting flux derived from FAST data and a cusp signature, *J. Geophys. Res. Space Physics*, 119, 411–430, doi:10.1002/2013JA019105.
- Cousins, E. D. P., T. Matsuo, and A. D. Richmond (2013a), Mesoscale and large-scale variability in high-latitude ionospheric convection: Dominant modes and spatial/temporal coherence, *J. Geophys. Res. Space Physics*, 118, 7895–7904, doi:10.1002/2013JA019319.
- Cousins, E. D. P., T. Matsuo, and A. D. Richmond (2013b), SuperDARN assimilative mapping, *J. Geophys. Res. Space Physics*, 118, 7954–7962, doi:10.1002/2013JA019321.
- Cousins, E. D. P., T. Matsuo, A. D. Richmond, and B. J. Anderson (2015a), Dominant modes of variability in large-scale Birkeland currents, *J. Geophys. Res. Space Physics*, 120, 6722–6735, doi:10.1002/2014JA020462.
- Cousins, E. D. P., T. Matsuo, and A. D. Richmond (2015b), Mapping high-latitude ionospheric electrodynamics with SuperDARN and AMPERE, *J. Geophys. Res. Space Physics*, 120, 5854–5870, doi:10.1002/2014JA020463.
- Davies, J., and M. Lester (1998), The relationship between electric fields, conductances and currents in the high-latitude ionosphere: A statistical study using EISCAT data, *Ann. Geophys.*, 17(1), 43–52, doi:10.1007/s00585-999-0043-3.
- Demmel, J. W. (1997), *Applied Numerical Linear Algebra*, Soc. for Ind. and Appl. Math., Philadelphia, Pa.
- Elphinstone, R. D., J. S. Murphree, and L. L. Cogger (1996), What is a global auroral substorm?, *Rev. Geophys.*, 34(2), 169–232, doi:10.1029/96RG00483.
- Emery, B., D. Evans, M. Greer, E. Holeman, K. Kadinsky-Cade, F. Rich, and W. Xu (2006), Low energy auroral electron and ion hemispheric power after NOAA and DMSP intersatellite adjustments, *Tech. Rep. NCAR/TN-470+STR*, Natl. Cent. for Atmos. Res., High Altitude Observatory (HAO), Boulder, Colo.
- Frey, H. U., S. B. Mende, V. Angelopoulos, and E. F. Donovan (2004), Substorm onset observations by IMAGE-FUV, *J. Geophys. Res.*, 109, A10304, doi:10.1029/2004JA010607.
- Fujii, R., R. A. Hoffman, P. C. Anderson, J. D. Craven, M. Sugiura, L. A. Frank, and N. C. Maynard (1994), Electrodynamic parameters in the nighttime sector during auroral substorms, *J. Geophys. Res.*, 99(A4), 6093–6112, doi:10.1029/93JA02210.
- Fuller-Rowell, T. J., and D. S. Evans (1987), Height-integrated Pedersen and Hall conductivity patterns inferred from the TIROS-NOAA satellite data, *J. Geophys. Res.*, 92(A7), 7606–7618, doi:10.1029/JA092iA07p07606.
- Galand, M., and A. D. Richmond (2001), Ionospheric electrical conductances produced by auroral proton precipitation, *J. Geophys. Res.*, 106(A1), 117–125, doi:10.1029/1999JA002001.
- Germany, G. A., D. G. Torr, P. G. Richards, M. R. Torr, and S. John (1994), Determination of ionospheric conductivities from FUV auroral emissions, *J. Geophys. Res.*, 99(A12), 23,297–23,305, doi:10.1029/94JA02038.
- Gjerloev, J. W., and R. A. Hoffman (2002), Currents in auroral substorms, *J. Geophys. Res.*, 107(A8), 1163, doi:10.1029/2001JA000194.
- Gjerloev, J. W., R. A. Hoffman, J. B. Sigwarth, and L. A. Frank (2007), Statistical description of the bulge-type auroral substorm in the far ultraviolet, *J. Geophys. Res.*, 112, A07213, doi:10.1029/2006JA012189.
- Hannachi, A., I. T. Jolliffe, and D. B. Stephenson (2007), Empirical orthogonal functions and related techniques in atmospheric science: A review, *Int. J. Climatol.*, 27(9), 1119–1152, doi:10.1002/joc.1499.
- Hardy, D. (1985), A statistical model of auroral electron precipitation, *J. Geophys. Res.*, 90(A5), 4229–4248.
- Hardy, D. A., L. K. Schmidt, M. S. Gussenhoven, F. J. Marshall, H. C. Yeh, T. L. Shumaker, A. Huber, and J. Pantazis (1984), Precipitating electron and ion detectors (SSJ/4) for the Block 5D/flights 6-10 DMSP satellites: Calibration and data presentation, *AFJ-TR-84-0317*, Air Force Geophys. Lab., Hanscom Air Force Base, Mass.
- Hardy, D. A., M. S. Gussenhoven, R. Raistrick, and W. J. McNeil (1987), Statistical and functional representations of the pattern of auroral energy flux, number flux, and conductivity, *J. Geophys. Res.*, 92(A11), 12,275–12,294, doi:10.1029/JA092iA11p12275.
- Hardy, D. A., E. G. Holeman, W. J. Burke, L. C. Gentile, and K. H. Bounar (2008), Probability distributions of electron precipitation at high magnetic latitudes, *J. Geophys. Res.*, 113, A06305, doi:10.1029/2007JA012746.
- Iijima, T., and T. A. Potemra (1978), Large-scale characteristics of field-aligned currents associated with substorms, *J. Geophys. Res.*, 83(A2), 599–615, doi:10.1029/JA083iA02p00599.
- James, G. M., T. J. Hastie, and C. A. Sugar (2000), Principal component models for sparse functional data, *Biometrika*, 87, 587–602.
- Jolliffe, I. (2002), *Principal Component Analysis*, 2nd ed., Springer, New York, doi:10.1007/b98835.
- Kadinsky-Cade, K., E. G. Holeman, J. McGarrity, F. J. Rich, W. F. Denig, W. J. Burke, and D. A. Hardy (2004), First results from the SSJ5 precipitating particle sensor on DMSP F16: Simultaneous observation of keV and MeV particles during the 2003 Halloween storms, *Eos Trans. AGU*, 85(17), Jt. Assem. Suppl., Abstract SH53A–03.
- Kamide, Y., and S. Kokubun (1996), Two-component auroral electrojet: Importance for substorm studies, *J. Geophys. Res.*, 101(A6), 13,027–13,046, doi:10.1029/96JA00142.
- Kamide, Y., and A. D. Richmond (1982), Ionospheric conductivity dependence of electric fields and currents estimated from ground magnetic observations, *J. Geophys. Res.*, 87(A10), 8331–8337, doi:10.1029/JA087iA10p08331.
- Kamide, Y., A. D. Richmond, and S. Matsushita (1981), Estimation of ionospheric electric fields, ionospheric currents, and field-aligned currents from ground magnetic records, *J. Geophys. Res.*, 86(A2), 801–813, doi:10.1029/JA086iA02p00801.

- Kamide, Y., J. D. Craven, L. A. Frank, B.-H. Ahn, and S.-I. Akasofu (1986), Modeling substorm current systems using conductivity distributions inferred from DE auroral images, *J. Geophys. Res.*, *91*(A10), 11,235–11,256, doi:10.1029/JA091iA10p11235.
- Kamide, Y., Y. Ishihara, T. L. Killeen, J. D. Craven, L. A. Frank, and R. A. Heelis (1989), Combining electric field and aurora observations from DE 1 and 2 with ground magnetometer records to estimate ionospheric electromagnetic quantities, *J. Geophys. Res.*, *94*(A6), 6723–6738, doi:10.1029/JA094iA06p06723.
- Kamide, Y., W. Sun, and S.-I. Akasofu (1996), The average ionospheric electrodynamic for the different substorm phases, *J. Geophys. Res.*, *101*(A1), 99–109, doi:10.1029/95JA02990.
- Kepko, L., R. McPherron, O. Amm, S. Apatenkov, W. Baumjohann, J. Birn, M. Lester, R. Nakamura, T. Pulkkinen, and V. Sergeev (2014), Substorm current wedge revisited, *Space Sci. Rev.*, *190*, 1–46, doi:10.1007/s11214-014-0124-9.
- Kihn, E. A., and A. J. Ridley (2005), A statistical analysis of the assimilative mapping of ionospheric electrodynamic auroral specification, *J. Geophys. Res.*, *110*, A07305, doi:10.1029/2003JA010371.
- Knipp, D. J. (1989), Quantifying and reducing uncertainty in the assimilative mapping of ionospheric electrodynamic, PhD thesis, Dep. of Atmospheric Sciences, Univ. of Calif., Los Angeles.
- Kozelov, B. V., I. V. Golovchanskaya, A. A. Ostapenko, and Y. V. Fedorenko (2008), Wavelet analysis of high-latitude electric and magnetic fluctuations observed by the Dynamic Explorer 2 satellite, *J. Geophys. Res.*, *113*, A03308, doi:10.1029/2007JA012575.
- Lei, J., et al. (2007), Comparison of COSMIC ionospheric measurements with ground-based observations and model predictions: Preliminary results, *J. Geophys. Res.*, *112*, A07308, doi:10.1029/2006JA012240.
- Lei, J., T. Matsuo, X. Dou, E. Sutton, and X. Luan (2012), Annual and semiannual variations of thermospheric density: EOF analysis of CHAMP and GRACE data, *J. Geophys. Res.*, *117*, A01310, doi:10.1029/2011JA017324.
- Lotko, W., R. H. Smith, B. Zhang, J. E. Ouellette, O. J. Brambles, and J. G. Lyon (2014), Ionospheric control of magnetotail reconnection, *Science*, *345*(6193), 184–187, doi:10.1126/science.1252907.
- Lummerzheim, D., M. Rees, J. Craven, and L. Frank (1991), Ionospheric conductances derived from DE-1 auroral images, *J. Atmos. Terr. Phys.*, *53*(3–4), 281–292, doi:10.1016/0021-9169(91)90112-K. Ionospheric Signatures of Magnetospheric Phenomena.
- Matsuo, T., A. D. Richmond, and D. W. Nychka (2002), Modes of high-latitude electric field variability derived from DE-2 measurements: Empirical orthogonal function (EOF) analysis, *Geophys. Res. Lett.*, *29*(7), 1107, doi:10.1029/2001GL014077.
- Matsuo, T., A. D. Richmond, and G. Lu (2005), Optimal interpolation analysis of high-latitude ionospheric electrodynamic using empirical orthogonal functions: Estimation of dominant modes of variability and temporal scales of large-scale electric fields, *J. Geophys. Res.*, *110*, A06301, doi:10.1029/2004JA010531.
- McGranaghan, R., D. J. Knipp, S. C. Solomon, and X. Fang (2015), A fast, parameterized model of upper atmospheric ionization rates, chemistry, and conductivity, *J. Geophys. Res. Space Physics*, *120*, 4936–4949, doi:10.1002/2015JA021146.
- McIntosh, R. C., and P. C. Anderson (2014), Maps of precipitating electron spectra characterized by Maxwellian and kappa distributions, *J. Geophys. Res. Space Physics*, *119*, 10,116–10,132, doi:10.1002/2014JA020080.
- McPherron, R. L., C. T. Russell, and M. P. Aubry (1973), Satellite studies of magnetospheric substorms on August 15, 1968: 9. Phenomenological model for substorms, *J. Geophys. Res.*, *78*(16), 3131–3149, doi:10.1029/JA078i016p03131.
- Nagata, T., and N. Fukushima (1971), Morphology of magnetic disturbance, *Handbuch der Physik*, *49*, 5–130.
- Nagy, A. F., and P. M. Banks (1970), Photoelectron fluxes in the ionosphere, *J. Geophys. Res.*, *75*(31), 6260–6270, doi:10.1029/JA075i031p06260.
- Newell, P. T., and J. W. Gjerloev (2011a), Evaluation of SuperMAG auroral electrojet indices as indicators of substorms and auroral power, *J. Geophys. Res.*, *116*, A12211, doi:10.1029/2011JA016779.
- Newell, P. T., and J. W. Gjerloev (2011b), Substorm and magnetosphere characteristic scales inferred from the SuperMAG auroral electrojet indices, *J. Geophys. Res.*, *116*, A12232, doi:10.1029/2011JA016936.
- Newell, P. T., and J. W. Gjerloev (2012), SuperMAG-based partial ring current indices, *J. Geophys. Res.*, *117*, A05215, doi:10.1029/2012JA017586.
- Newell, P. T., C.-I. Meng, and K. M. Lyons (1996a), Suppression of discrete aurorae by sunlight, *Nature*, *381*, 766–767, doi:10.1038/381766a0.
- Newell, P. T., K. M. Lyons, and C.-I. Meng (1996b), A large survey of electron acceleration events, *J. Geophys. Res.*, *101*(A2), 2599–2614, doi:10.1029/95JA03147.
- Newell, P. T., T. Sotirelis, K. Liou, C.-I. Meng, and F. J. Rich (2007), A nearly universal solar wind-magnetosphere coupling function inferred from 10 magnetospheric state variables, *J. Geophys. Res.*, A01206, doi:10.1029/2006JA012015.
- Newell, P. T., T. Sotirelis, and S. Wing (2009), Diffuse, monoenergetic, and broadband aurora: The global precipitation budget, *J. Geophys. Res.*, *114*, A09207, doi:10.1029/2009JA014326.
- Nicolls, M. J., R. Cosgrove, and H. Bahcivan (2014), Estimating the vector electric field using monostatic, multibeam incoherent scatter radar measurements, *Radio Sci.*, *49*, 1124–1139, doi:10.1002/2014RS005519.
- Opgenoorth, H. J., M. A. L. Persson, T. I. Pulkkinen, and R. J. Pellinen (1994), Recovery phase of magnetospheric substorms and its association with morning-sector aurora, *J. Geophys. Res.*, *99*(A3), 4115–4129, doi:10.1029/93JA01502.
- Pearson, K. (1901), On lines and planes of closest fit to systems of points in space, *Philos. Mag.*, *2*(6), 559–572.
- Pellinen, R., T. Pulkkinen, and K. Kauristie (1994), Have we learned enough about auroral substorm morphology during the past 30 Years?, in *Proceedings of the Second International Conference on Substorms*, 43–48, Fairbanks, Alaska, 7–11 March.
- Picone, J. M., A. E. Hedin, D. P. Drob, and A. C. Aikin (2002), NRLMISE-00 empirical model of the atmosphere: Statistical comparisons and scientific issues, *J. Geophys. Res.*, *107*(A12), 1468, doi:10.1029/2002JA009430.
- Provan, G., M. Lester, S. B. Mende, and S. E. Milan (2004), Statistical study of high-latitude plasma flow during magnetospheric substorms, *Ann. Geophys.*, *22*(10), 3607–3624, doi:10.5194/angeo-22-3607-2004.
- Pytte, T., R. McPherron, and S. Kokubun (1976), The ground signatures of the expansion phase during multiple onset substorms, *Planet. Space Sci.*, *24*(12), 1115–1132, doi:10.1016/0032-0633(76)90149-5.
- Redmon, R. J., J. V. Rodriguez, J. C. Green, D. Ober, G. Wilson, D. Knipp, L. Kilcommons, and R. McGuire (2015), Improved polar and geosynchronous satellite data sets available in common data format at the coordinated data analysis web, *Space Weather*, *13*, 254–256, doi:10.1002/2015SW001176.
- Reiff, P. H. (1984), Models of auroral-zone conductances, in *Magnetospheric Currents*, edited by T. A. Potemra, pp. 180–191, AGU, Washington, D. C., doi:10.1029/GM028p0180.
- Rich, F. J., D. D. Hardy, and M. S. Gussenhoven (1985), Enhanced ionosphere-magnetosphere data from the DMSP satellites, *Eos Trans. AGU*, *66*(26), 513–514, doi:10.1029/EO066i026p00513.
- Richards, P. G., D. Bilitza, and D. Voglozin (2010), Ion density calculator (IDC): A new efficient model of ionospheric ion densities, *Radio Sci.*, *45*, RS5007, doi:10.1029/2009RS004332.

- Richmond, A. D., and Y. Kamide (1988), Mapping electrodynamic features of the high-latitude ionosphere from localized observations: Technique, *J. Geophys. Res.*, *93*(A6), 5741–5759, doi:10.1029/JA093iA06p05741.
- Ridley, A. J., T. I. Gombosi, and D. L. DeZeeuw (2004), Ionospheric control of the magnetosphere: Conductance, *Ann. Geophys.*, *22*(2), 567–584, doi:10.5194/angeo-22-567-2004.
- Robinson, R. M., and R. R. Vondrak (1984), Measurements of E region ionization and conductivity produced by solar illumination at high latitudes, *J. Geophys. Res.*, *89*(A6), 3951–3956, doi:10.1029/JA089iA06p03951.
- Robinson, R. M., R. R. Vondrak, K. Miller, T. Dabbs, and D. Hardy (1987), On calculating ionospheric conductances from the flux and energy of precipitating electrons, *J. Geophys. Res.*, *92*(A3), 2565–2569, doi:10.1029/JA092iA03p02565.
- Roble, R. G., E. C. Ridley, A. D. Richmond, and R. E. Dickinson (1988), A coupled thermosphere/ionosphere general circulation model, *Geophys. Res. Lett.*, *15*(12), 1325–1328, doi:10.1029/GL015i012p01325.
- Sandford, P. (1968), Variations of auroral emissions with time, magnetic activity and the solar cycle, *J. Atmos. Terr. Phys.*, *30*(12), 1921–1942, doi:10.1016/0021-9169(68)90001-9.
- Schreiner, W., C. Rocken, S. Sokolovskiy, S. Syndergaard, and D. Hunt (2007), Estimates of the precision of GPS radio occultations from the COSMIC/FORMOSAT-3 mission, *Geophys. Res. Lett.*, *34*, L04808, doi:10.1029/2006GL027557.
- Schunk, R., and A. Nagy (2009), *Ionospheres: Physics, Plasma Physics, and Chemistry*, Cambridge Atmos. and Space Sci. Ser., Cambridge Univ. Press, Cambridge, U. K.
- Sergeev, V. A., L. I. Vagina, R. D. Elphinstone, J. S. Murphree, D. J. Hearn, L. L. Cogger, and M. L. Johnson (1996), Comparison of UV optical signatures with the substorm current wedge as predicted by an inversion algorithm, *J. Geophys. Res.*, *101*(A2), 2615–2627, doi:10.1029/95JA00537.
- Solomon, S. C., and V. J. Abreu (1989), The 630 nm dayglow, *J. Geophys. Res.*, *94*(A6), 6817–6824, doi:10.1029/JA094iA06p06817.
- Solomon, S. C., P. B. Hays, and V. J. Abreu (1988), The auroral 6300 Å emission: Observations and modeling, *J. Geophys. Res.*, *93*(A9), 9867–9882, doi:10.1029/JA093iA09p09867.
- Strobel, D., C. Opal, and R. Meier (1980), Photoionization rates in the night-time E- and F-region ionosphere, *Planet. Space Sci.*, *28*(11), 1027–1033, doi:10.1016/0032-0633(80)90050-1.
- Thorne, R. M., B. Ni, X. Tao, R. B. Horne, and N. P. Meredith (2010), Scattering by chorus waves as the dominant cause of diffuse auroral precipitation, *Nature*, *467*(7318), 943–946, doi:10.1038/nature09467.
- Tibshirani, R. (1996), Regression shrinkage and selection via the Lasso, *J. R. Stat. Soc., Ser. B*, *58*, 267–288.
- Wilks, D. (2011), *Statistical Methods in the Atmospheric Sciences*, vol. 100, 2nd ed., Academic Press, Ithaca, N. Y., doi:10.1016/B978-0-12-385022-5.00022-1.
- Wiltberger, M., R. S. Weigel, W. Lotko, and J. A. Fedder (2009), Modeling seasonal variations of auroral particle precipitation in a global-scale magnetosphere-ionosphere simulation, *J. Geophys. Res.*, *114*, A01204, doi:10.1029/2008JA013108.
- Winningham, J. D., F. Yasuhara, S. I. Akasofu, and W. J. Heikkila (1975), The latitudinal morphology of 10-eV to 10-keV electron fluxes during magnetically quiet and disturbed times in the 2100-0300 MLT sector, *J. Geophys. Res.*, *80*(22), 3148–3171, doi:10.1029/JA080i022p03148.
- Zhang, B.-C., Y. Kamide, R.-Y. Liu, H. Shinagawa, and K. Iwamasa (2004), A modeling study of ionospheric conductivities in the high-latitude electrojet regions, *J. Geophys. Res.*, *109*, A04310, doi:10.1029/2003JA010181.
- Zhou, X. W., C. T. Russell, G. Le, S. A. Fuselier, and J. D. Scudder (2000), Solar wind control of the polar cusp at high altitude, *J. Geophys. Res.*, *105*(A1), 245–251, doi:10.1029/1999JA900412.